Constraining the depth extent of low-velocity zone along the Chenghai Fault by dense array ambient noise interferometry and horizontal-to-vertical spectral ratio

Yuyang She [a], Huajian Yao [a,b,c,*], Hongfeng Yang [d,e,**], Juanjuan Wang [a], Jikun Feng [a]

[a] *Laboratory of Seismology and Physics of Earth's Interior, School of Earth and Space Sciences, University of Science and Technology of China, Hefei, China*
[b] *CAS Center for Excellence in Comparative Planetology, University of Science and Technology of China, Hefei 230026, China*
[c] *Mengcheng National Geophysical Observatory, University of Science and Technology of China, Mengcheng, China*
[d] *Earth System Science Programme, The Chinese University of Hong Kong, Sha Tin, NT, Hong Kong, China*
[e] *Shenzhen Research Institute, The Chinese University of Hong Kong, Shenzhen, Guangdong, China*

ARTICLE INFO

ABSTRACT

The depth extent of low velocity fault zones is still a matter of debate due to the lack of vertical resolution for most seismic methods. Autocorrelations and cross-correlations of seismic ambient noise provide us new constraints on this issue by obtaining the shallow subsurface reflections without the need of active sources or earthquakes. The horizontal-to-vertical spectral ratio (HVSR) method can also give constraints on this interface and does not need any extra cost of data collection. In this study, we used one-month continuous seismic data from a dense linear array deployed crossing the Chenghai Fault (CHF) in Yunnan, southwest China. Single station autocorrelation and adjacent station pair cross-correlation methods were used to retrieve body wave reflections from the interface of the shallow crustal low-velocity zone (LVZ). The HVSR method was also performed to delineate the shape of the LVZ. Results show an inverted trapezoidal LVZ which extends to ~1.0 km depth across the fault zone with a lateral extent of ~3 km. Previous studies based on ambient noise surface-wave tomography and teleseismic travel time analysis in the same area show similar characteristics, consistent with the interpretation of our results.

1. Introduction

Crustal faults are generally associated with damaged zones that have intensive fractures around the main slip surface (Ben-Zion and Sammis, 2003; Yang et al., 2014; Yang et al., 2021). Generally, the damaged zone is generated by earthquakes over time and is seismically characterized as a low-velocity zone (LVZ) with a reduction in seismic velocities relative to the host rocks (Ben-Zion and Sammis, 2009; Yang and Zhu, 2010). High-resolution imaging of fault zone structure has great significance for us to understand the earthquake physics and provide important constraints on the behavior of past and future earthquakes on the fault. Based on high-resolution models, we can conduct numerical simulations for earthquake generation, rupture propagation, ground motion, slip localization, and so on. These approaches can give us an intuitive understanding of earthquake physics and behaviors. Several investigations

have been made to obtain high-resolution images of fault zone structures. These include direct geological mapping and analysis of fault zone samples (e.g., Chester et al., 1993; Li et al., 2013), body wave travel time tomography (e.g., Thurber et al., 2006; Allam and Ben-Zion, 2012), ambient seismic noise tomography (e.g., Zhang and Gerstoft, 2014; Zigone et al., *2014*; Vassallo et al., 2016; Zigone et al., 2019; Gu et al., 2019; Yang et al., 2020; Qian and Liu, 2020; Li et al., 2020) and waveform modeling of fault zone related seismic phases (Ben-Zion and Malin, 1991; Li et al., 2007; Yang and Zhu, 2010; Hillers et al., 2014). Despite the past efforts on imaging high-resolution fault zone structure, the depth extent of LVZ is still a big challenge due to the lack of vertical resolution (Yang, 2015).

A potentially good constraint on the depth extent of the LVZ is provided by exploiting stacked autocorrelograms or cross-correlograms of the continuous seismic records. Similar to the receiver function

---

technique, the correlation methods are sensitive to the interface and thus can provide a robust constraint on the LVZ depth. Furthermore, these methods don't need any active source, earthquakes, or long-term data collection, and therefore have already been successfully applied to retrieve P wave reflections for different scale imaging in different areas (Kennett et al., 2015; Taylor et al., 2016; Feng et al., 2017; Saygin et al., 2017; Romero and Schimmel, 2018).

Besides, the Horizontal-to-Vertical Spectral Ratio (HVSR) method is another potentially efficient way to constrain the depth extent of LVZ (Nakamura, 1989; Bonnefoy-Claudet et al., 2006; Sánchez-Sesma et al., 2011). We can extract the frequency responses for the sharp seismic impedance between the sediment and basement through HVSR curves. Benefiting from its efficiency, the HVSR method has been widely used to investigate the shallow structure, especially within basins (Parolai et al., 2002; Bao et al., 2018; Molnar et al., 2018).

Here we aim to image the high-resolution structure of the Chenghai Fault (CHF) in western Yunnan, China. The CHF is a ~ 200 km long left-lateral strike-slip system, accompanied by normal dip-slip faulting. The CHF formed in the Prepaleozoic Era and extends from Yongsheng in the north to the Binchuan basin in the south. Not only the CHF, but many other faults with different trending and movement patterns are also distributed in this area. They have accommodated significant tectonic deformation and posed serious seismic hazards in this region (Allen et al., 1984). The largest earthquake that occurred on the CHF was the 1515 M7.7 Yongsheng earthquake (Huang et al., 2018a). According to the positive correlation between the intensity of seismic and fault activities, former studies considered the Binchuan area as an M7.0 earthquake potential area (Huang et al., 2018b). Yang et al. (2020) derive the high-resolution velocity structure of the CHF from records on a dense linear array crossing the fault. They found a LVZ of ~3.4 km in width and ~ 1.5 km in depth through ambient noise tomography. However, the model-predicted S wave arrivals are delayed in comparison with observations, suggesting that the depth extent of the LVZ was probably

overestimated because of limited depth resolution in the LVZ. This inference has been proved in the newly developed array-based receiver function images (Jiang et al., 2021).

In this work, we applied the correlation methods and HVSR technique to our study region, the CHF in Yunnan, China. It is the first time that we calculate the autocorrelograms and cross-correlograms to retrieve body wave reflections from such a dense array. Previous studies based on correlation methods used stations separated by a few kilometers to several hundred kilometers. In comparison, the dense linear array we used has a small averaged spacing of ~50 m. It can provide us better constraints on the depth extent and lateral variation of the LVZ in CHF from these two kinds of methods.

2. Data and method

Between January 2018 and February 2018, 125 three-component short-period seismometers were installed across the CHF in the Binchuan basin, Yunnan Province, southwest China (Yang et al., 2020). The instrument has a built-in battery and data logger and a corner frequency of 5 s for all three components. These stations are in a roughly linear grid with an approximate station spacing of ~50 m (Fig. 1). Continuous recordings were collected at each point with 100 Hz sampling. This very dense linear array provides a great opportunity to image the high-resolution structure of the CHF area and to constrain the depth extent of the LVZ.

2.1. Ambient noise interferometry

Retrieving the Earth's reflection response by seismic interferometry involves three steps: pre-processing the recorded ambient seismic noise, computing autocorrelations or cross-correlations of the preprocessed data, and stacking of the correlation functions.

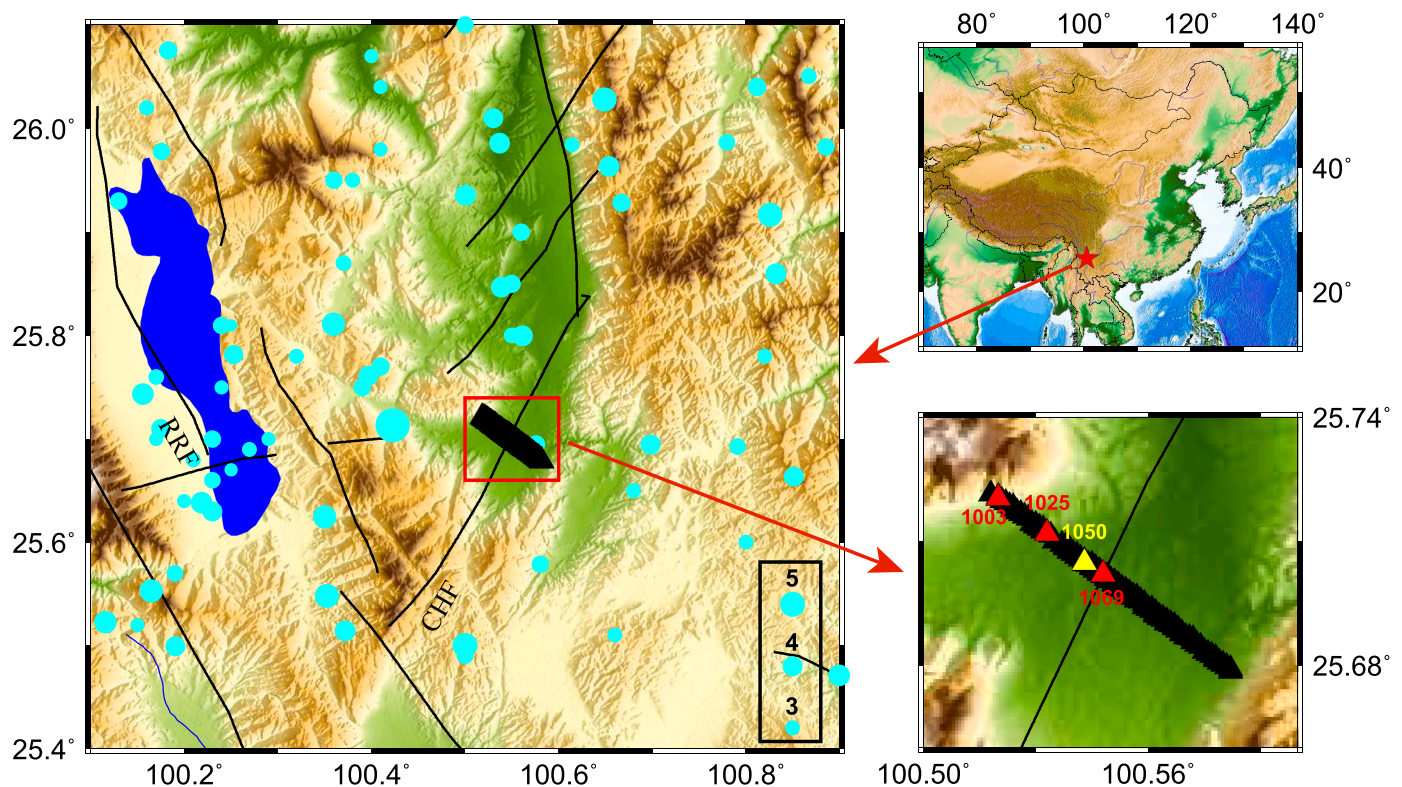For the initial pre-processing of ambient noise data, the instrument

Fig. 1. Geological map and seismicity of the study area and the location of the short-period seismometers. Those stations used in other figures are also marked in the figure. RRF: Red River fault, CHF: Chenghai fault. (For interpretation of the references to colour in this figure legend, the reader is referred to the web version of this article.)

response was first removed. The data were then cut to 1-day lengths, with mean and linear trends removed. The power spectra of the pre-processed ambient noise are not flat and are dominated by primary and secondary microseism peaks primarily generated by ocean waves (Bensen et al., 2007). All the segments were band-pass filtered between 1 Hz and 2 Hz to enhance the reflectivity information beneath the stations. Moreover, energetic signals such as earthquakes, instrument malfunction, and local noise will also dominate the correlations (Bensen et al., 2007). In order to avoid contamination and bias from those high-amplitude signals, we applied time-domain normalization and spectral whitening with the running absolute mean method.

After the preparation of the daily time-series described below, the next step is computing the correlation functions. Correlation is a mathematical process that is often used to measure the similarity between two time series. In this work, we used the traditional correlation method based on the highest signal-to-noise ratio. We also tested other cross-correlation methods such as phase correlations (Schimmel et al., 2011).

Finally, correlation functions were stacked to improve the coherent reflection signals and to suppress noise. Here we used the phase-weighted stacking method (PWS) (Schimmel and Paulssen, 1997) because of its high efficiency in suppressing noise. To do so, the daily correlation functions were Hilbert transformed to split the instantaneous phase functions. Then we weighted the linear stack signals by the instantaneous phase coherency to enhance the coherent signals.

Fig. 2a shows an example of cross-correlation functions between station 1050 and all other stations in the frequency band 1–4 Hz. A wider frequency band is used here to show more details about the P wave. Fig. 2b shows the noise correlations stacked by distance bin of 0.1 km length. It shows the stack of the positive and negative parts of the correlation functions filtered in the same range of 1–4 Hz. The surface waves are dominant in the correlation functions. Although the refracted P waves can be observed, the reflected phases are hard to distinguish. The surface waves tend to mask possible reflections except in near-zero offset windows. In order to avoid the influence of surface waves, we used single-station autocorrelations and adjacent station pair cross-correlations to obtain the shallow subsurface reflection response.

2.2. The HVSR method

The HVSR method can help us retrieve and evaluate the resonance frequencies of unconsolidated sediments over high-velocity bedrocks (e. g., Chandler and Lively, 2016; Molnar et al., 2018). Following Nakamura (1989) and Arai and Tokimatsu (2004), we can express the H/V spectral ratio of microtremors at a frequency f as

$$\text{HVSR}(f) = \sqrt{\frac{NS(f)^2 + EW(f)^2}{V(f)^2}} \qquad (1)$$

where $V(f)$ is the Fourier power spectrum of the vertical motion and $NS(f)$ and $EW(f)$ are those of the two horizontal motions. We computed the HVSR curve of each station with the following procedure.

First, we split the entire three-component continuous data into several time windows of equal length. Window length is inversely proportional to the minimum frequency, so longer time windows should be used to measure stable low-frequency results. To extract HVSR in 0.2 Hz, daily seismic records were cut into 50 s-long time windows. We also performed statistical analysis for each time window and remove outlier windows in which the amplitude is in non-Gaussian distribution. Then we computed the Fourier spectra and the H/V ratio for each time window. We calculated the mean and standard deviation of each frequency for all time windows. The time windows were also removed if the corresponding HVSR curves have more than one third of frequency points out of two standard deviations. Finally, the HVSR curves from all left time windows were stacked to derive the averaged HVSR curve.

3. Results

3.1. P wave reflectivity profile from correlation methods

Due to the low amplitude of body wave reflections in the ambient noise field, we can only retrieve reflections from the interface representing relatively strong contrasts in material properties, such as velocity and density. Our results of autocorrelations and cross-correlations show clear reflections from the bottom boundary of the LVZ. All traces were filtered with a band-pass filter between 1 and 2 Hz, and a cosine taper was applied to suppress the characteristic zero-time peak. Higher-frequency noise sources would be able to increase the vertical resolution of this approach, but the ambient noise field recorded at this linear array contains little power at frequencies >5 Hz.

For each station, we computed the autocorrelations for the 1-day segment with the maximum time lag up to 20 s. An example of the daily autocorrelations for station 1050 located in the central part of the CHF is shown in Fig. 3a. We also stacked the autocorrelograms by linear and phase-weighted stacking methods. The results were quite similar (Fig. 3a). In fact, it is quite difficult to identify the reflection signals by using the result from a single station due to the interference of noise such as multiples. But we can still find out the most likely reflection signals through some simple rules. First, the reflection signals should have larger amplitude than noise or multiples. Second, a positive impedance contrast corresponds to a negative phase in autocorrelograms. Third, the reflection signals from an interface should be a stable arrival during the
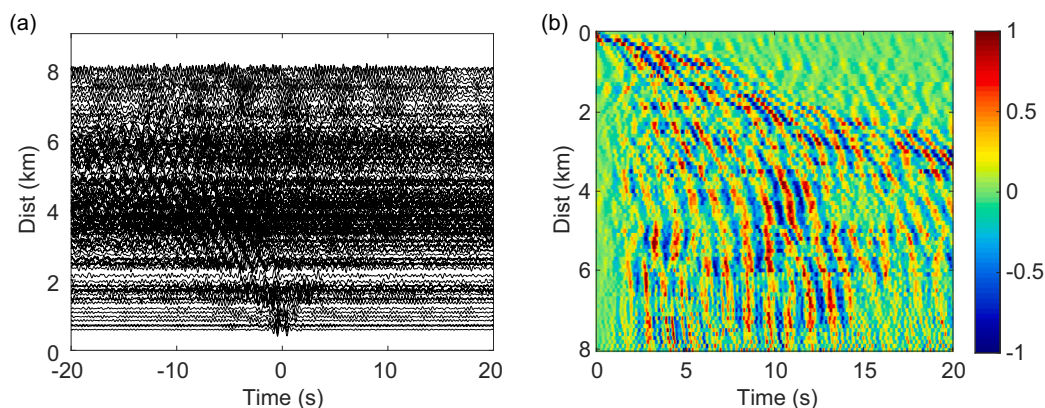

Fig. 2. (a) An example of cross-correlations between station 1050 with all other stations. (b) Stacked noise correlations using distance-averaged bins. Each bin is 0.1 km in the distance range. The autocorrelations are along the top edge (offset = 0) of this figure.
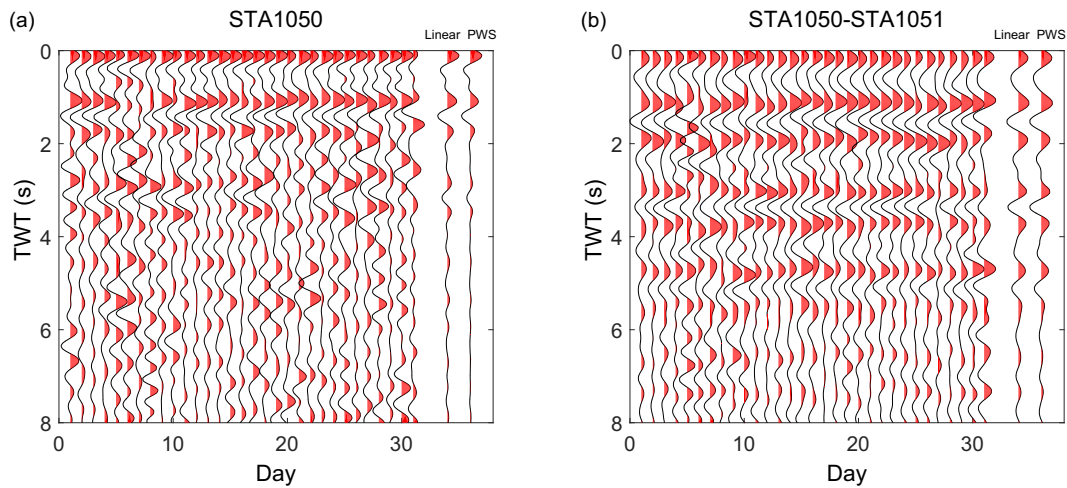
Fig. 3. Section plot of daily correlation functions computed with autocorrelation (a) and cross-correlation (b). The two traces to the right of each panel are the linear stack/phase-weighted stack of the autocorrelograms and cross-correlograms, respectively. *TWT = two-way time.*

entire operation time window. Based on these principles, we infer that the clear signal at ~1.5 s two-way traveltime (TWT) is the reflection response from a low-velocity boundary (Fig. 3a). The variation in the P wave arrival time is very small and the amplitude is stronger than any others. Another possible reflection is detected at ~3.1 s in autocorrelograms. In consideration of the similarity of the waveform, the double arrival time, and the smaller amplitude of this signal compared with the reflection at ~1.5 s, we interpret this signal as multiple reflections.

Similarly, we calculated the cross-correlations for each adjacent station pair (Fig. 3b). The corresponding reflections at cross-correlograms are found at ~1.6 s and ~ 3.3 s TWT. The difference in time for the reflections can be explained by the different principles of autocorrelation and cross-correlation. The cross-correlation of two stations turns one into a virtual source, whose signal is recorded at the other receiver, while the autocorrelation is equal to zero offset seismic records. At ~5 s in cross-correlograms appears another multiple reflection, but the amplitude is slightly diminished and the daily signals

are less robust compared to the signals at ~1.6 s and ~ 3.3 s (Fig. 3a).

After we got the daily autocorrelations (cross-correlations) for each station (station pair), all the individual autocorrelations (cross-correlations) were stacked to obtain one total stack per station (station pair) for final interpretation. The phase-weighted stack of autocorrelogram for each station and cross-correlograms for each station pair are shown in Fig. 4a and b, respectively. The x-axis is the distance between each station (or the midpoint of each station pair) and station 1001 (the northwest-most station). Results from such a dense linear array can help us identify the reflection signals. The result from a single station may be affected by noise and thus is less reliable. We can use the similarity from neighboring stations to reevaluate the signals and track the variations of the interface simultaneously.

Robust P wave reflections could be detected as isolated and clear signals for most of the stations, especially the stations in the central part of CHF (Fig. 4a&b). In combination with the results of ambient noise tomography (Yang et al., 2020), the most likely reflection from the
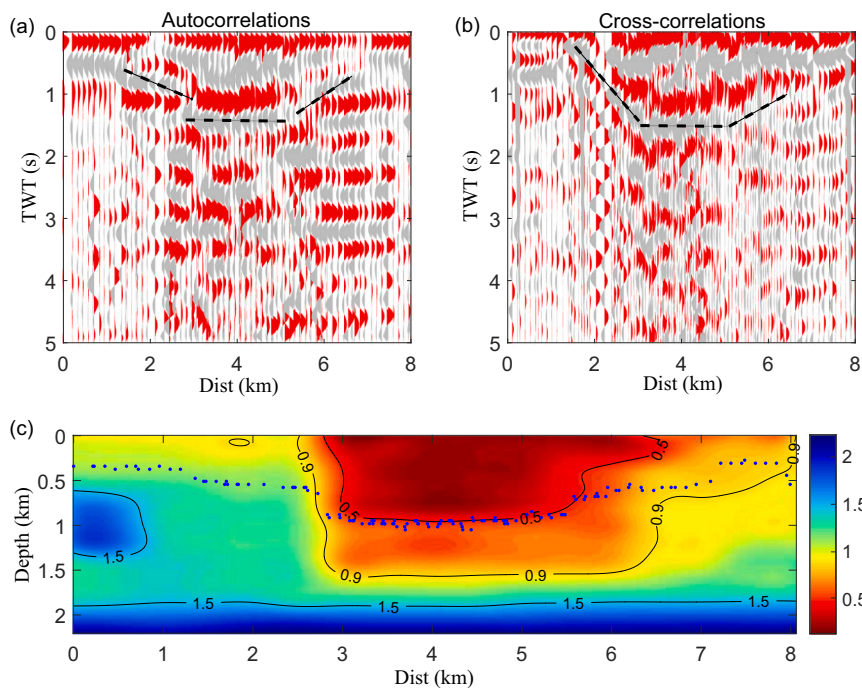

Fig. 4. Autocorrelations (a) and Cross-correlations (b) (to 5-s lag) at each station (from northwest to southeast) in the dense linear array. Positive amplitudes are in red. Polarity has not been changed and a negative polarity indicates a positive impedance contrast. The first large reflection, which we interpret as a reflection from the interface of LVZ, is marked by a dashed black line. (c) S wave velocity (km/s) derived from ambient noise surface wave tomography using the same stations as in this study (from Yang et al., 2020). The blue dots are the converted model from autocorrelation results. *TWT: two-way time.* (For interpretation of the references to colour in this figure legend, the reader is referred to the web version of this article.)

bottom boundary of the LVZ is marked by the black dash lines (Fig. 4c). We can see the whole LVZ is well captured by the dense linear array. Strong lateral variation of the interface indicates the boundary of the damaged zone (Fig. 4c). The reflection signals are sufficiently clear to be detected at distances from ~1.5 km to ~7 km and the reflected P wave arrival time varies from ~0.7 s to ~1.5 s. The TWT of the reflection gets larger at distances from ~1.5 km to ~2.8 km, and keeps the largest value at distances from ~3 km to ~5.5 km. Then the TWT becomes smaller until at distances ~7 km. The variation of the TWT reveals the variation of the depth extent of the LVZ.

3.2. Resonant frequency from HVSR method

The HVSR curves of all stations were computed for the potential information of the interface. Fig. 5 shows three examples of HVSR curves that represent three kinds of results. They have different numbers of resonant frequencies corresponding to different kinds of structure (Fig. 5a-c). Generally, the resonant frequency of the HVSR curve corresponds to the main interface of the sedimentary layer. No resonant frequency usually means no sharp impedance contrast between sediment and basement. The cause of two resonant frequencies is a bit more ambiguous. It might be a harmonic of the fundamental period, or might correspond to another layer (Bodin et al., 2001). However, the low-frequency peak is always significantly larger than the higher frequency peak. The HV curves of all 125 stations are normalized by amplitude and shown in Fig. 5d. We can clearly observe an inverted trapezoidal boundary in this figure. All resonant frequencies are picked manually and the station with different number of resonant frequencies are distinguished by the colour of their resonant frequencies (Fig. 5e).

Interestingly, we find that the central stations in the linear array all have two resonant frequencies. In contrast, the stations having single frequency peak are all distributed at the two ends of the linear array. This phenomenon might be caused by the structure difference between the fault zone and the surrounding area. The main resonant frequencies vary from ~0.1 to ~0.8 Hz, which implies the variation of the thickness of sediment.

3.3. Estimation on the depth of reflectors

In the previous seismic ambient noise tomography study of Yang et al. (2020), the S wave velocity of this area is estimated up to 1.5 km depth using surface waves extracted from interstation seismic noise cross-correlations (Fig. 4c). In this S wave velocity image, we find that the LVZ extends from ~2.8 km to ~6.5 km in width and ~ 1.5 km in depth. The shape of the LVZ is similar to our result. We further calculate the average P wave velocity in the LVZ to convert the TWT to depth by 1-D zero-offset ray tracing. This average P wave velocity is obtained from the S wave velocity model by assuming a constant Vp/Vs ratio of 2.25, similar to what was derived from receiver functions in the LVZ (Jiang et al., 2021). We choose this Vp/Vs ratio base on the empirical study of Brocher (2005) and Saygin et al. (2017). The converted model of the depth of the LVZ is plotted by blue dots in Fig. 4c. Our model obtained by the autocorrelation method shows the interface of the low-velocity boundary, which has good correspondence with the tomography model. The teleseismic travel time analysis (Yang et al., 2020) also shows similar characteristic, which provides strong evidence for our study.

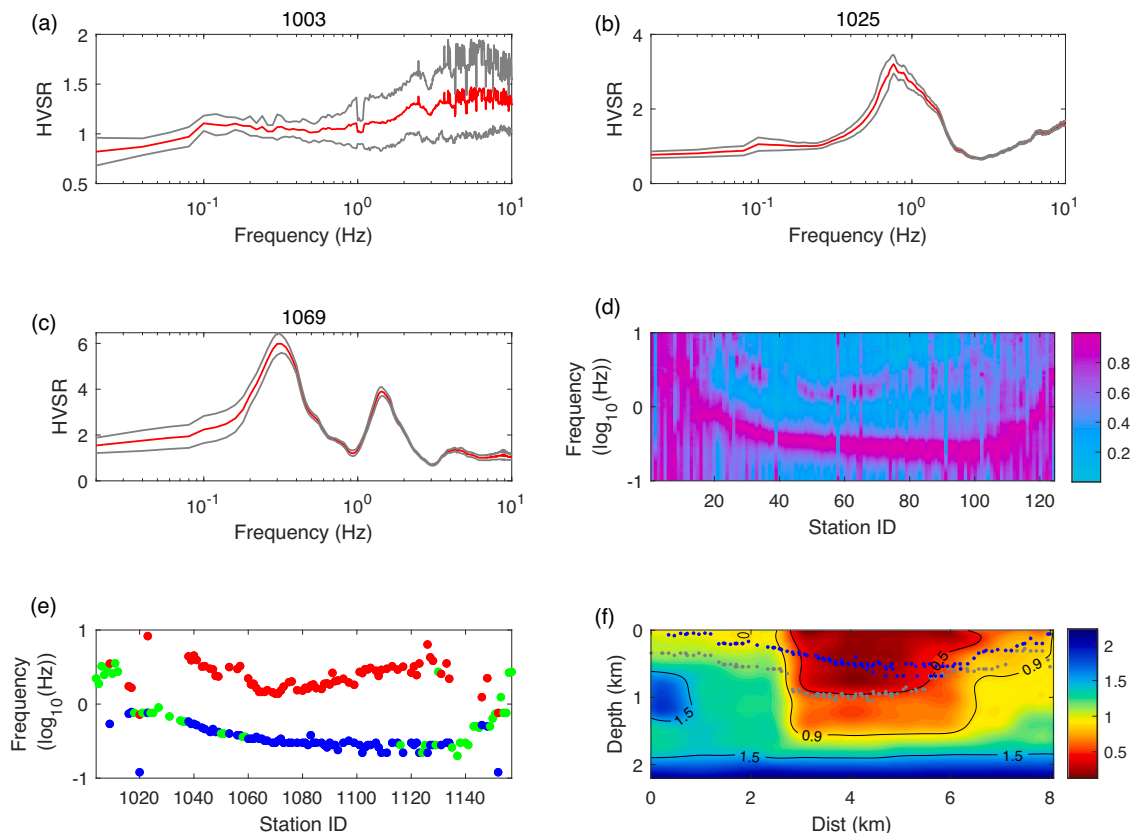For the simplest case of a uniform sediment layer, the relationship

Fig. 5. Three examples of HVSR results with no resonant frequency (a), one resonant frequency (b), and two resonant frequencies (c). The gray line represents the one standard deviation. (d) HV curves for all 125 stations after amplitude normalization for each station. (e) The resonant frequencies for all stations. Red and blue dots represent the two resonant frequencies of those stations which have two resonant frequencies. The green dots represent the resonant frequencies of those stations which have only one resonant frequency. (f) The comparison of converted model from autocorrelation results (blue dots) and HVSR results (gray dots). (For interpretation of the references to colour in this figure legend, the reader is referred to the web version of this article.)

between the resonant frequency *f* and the thickness *H* of the sediment layer can be determined as the following

$$H = \frac{Vs}{4f} \tag{2}$$

where *Vs* is the average S-wave velocity. But the S-wave velocities actually tend to increase nonlinearly with depth, due to compaction and other factors (Budny, 1985). In the absence of S-wave velocity information, Ibs-von Seht and Wohlenberg (1999) demonstrate that an empirical power-law relationship could be established between sediment thickness *H* and the resonant frequency *f* by

$$H = af^b \tag{3}$$

where parameters *a* and *b* are determined empirically by collecting data at control points such as drillholes. The parameters from the fitted power-law relationship can then be used to estimate thickness in areas without bedrock information.

Benefit from the S-wave velocity model established by Yang et al. (2020), we calculate the average S-wave velocity by using the traveltime information. Then the thickness of the LVZ can be estimated by eq. 2 (Fig. 5f). The boundary of the LVZ estimated from the HVSR method is shallower than autocorrelation results. To avoid the uncertainty from average velocity estimation, we further compare the f^{-1} of the HVSR method and TWT of the correlation methods directly to constrain the shape of the interface (Fig. 6). Results from the two kinds of methods match well and show a similar shape of the LVZ.

4. Discussion

We delineate a low-velocity boundary of the CHF region from dense array ambient noise interferometry and the HVSR method. An inverted trapezoidal LVZ which extends to ~1.0 km depth is shown in our results from two different methods. The formation and evolution of such wide and shallow LVZ along the CHF were under the combined effects of the regional EW-trending extension and the clockwise rotation of micromassifs in this area (Wang et al., 1998; Fan et al., 2006). The left-lateral and pull-apart tectonic movement pattern was driven by the holistic clockwise rotation of the Tibetan Plateau (Wang et al., 1998; Zhang et al., 2004; Shen et al., 2005). Strike-slip movement caused intensive fractures around the main slip surface and the EW-trending extensional movement increased the rupture in top of the fault zone.
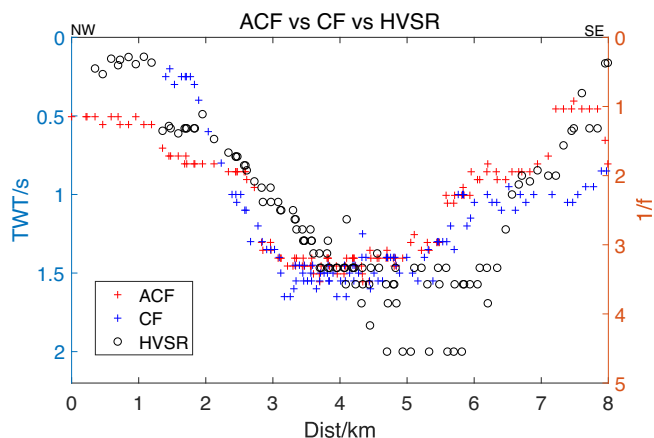
After a long-time geologic process of weather denudation and sedimentation on top of the fault zone, the inverted trapezoidal LVZ is gradually formed. The LVZ usually plays an important role in earthquake generation and rupture distribution (e.g., Dor et al., 2006; Ben-Zion and Ampuero, 2009; Huang et al., 2014; Yang and Yao, 2021). Cracks and fluids in the zone may decrease the strength of faults (Eberhart-Phillips et al., 1995; Faulkner et al., 2010) and the low-velocity material may amplify ground motion (Ben-Zion and Aki, 1990; Chen and Yang, 2020) and influence rupture propagation (Ben-Zion and Shi, 2005; Weng et al., 2016). Such a wide LVZ would be a significant potential risk of earthquake hazards for nearby residents.

Single-station autocorrelation and adjacent station pair cross-correlation methods were used to image the LVZ in the CHF area. These methods give a new approach to constrain the depth extent of the LVZ. In previous studies, fault zone trapped waves are commonly used to image the fault zone structure (Li et al., 1990; Ben-Zion and Sammis, 2003). Besides, seismic tomography methods are good ways to achieve high resolution of fault zone structure (Lin et al., 2013; Hillers et al., 2014; Zigone et al., 2019). But the vertical resolution of these methods is relatively low, which may lead to different conclusions in depth extent of the LVZ. The receiver function technique is a useful way to determine the interface but usually fails due to the reverberated phases in a low-velocity layer (Zelt and Ellis, 1999). Recently, Jiang et al. (2021) developed an array-based receive function technique, which can invert travel times of the LVZ and constrain subsurface structure. But in correlation methods, the reverberated wavefield reveals the effect of the low-velocity layer. So these methods can be good alternatives to detect the underground interfaces. Besides, the HVSR method we use can provide another constraint on the depth extent of LVZ. This method is also based on ambient noise data so that we can apply it to our study area without extra cost of data collection. In addition, these two kinds of methods can successfully detect the interface by using a few days of data and without the need for any active sources or earthquakes. For this study, only one month of continuous data was acquired and processed, but delivers confident results.

The thicknesses of the LVZ estimated from two methods are different, which shown in Fig. 5f. The largest error is expected from the time/frequency-to-depth conversions through inaccurate velocity models. For example, we used a traveltime-based average velocity in the HVSR method. However, this approach is established without taking into account the theory of the H/V ratio technique and it exhibits a flaw that the resonance frequency does not depend on the arrangement of the layers and their mass density (*Tuan* et al., 2016a & 2016b). The imperfect recovery of reflections due to even distribution of ambient noise sources is likely another source of uncertainty for the ambient noise interferometry method. Although the results from two different methods exhibit a gap in absolute values of the LVZ thickness, the shape of the LVZ from both methods is quite similar.

A difficulty in correlation methods we should mention is the contamination of sidelobes near zero time, which will affect early P wave arrivals. The sidelobes are caused by the convolution of a delta pulse at zero time lag with the effective noise source time function (e.g., Ruigrok and Wapenaar, 2012). Applying a cosine taper to suppress the zero-time peak is useful to reduce the influence of sidelobes. Fig. 7d gives an example of autocorrelation results without tapering. It can be seen that the arrivals are masked by the sidelobes compared with the result with a taper (Fig. 7a). Instead of using a cosine taper, the procedure proposed by Clayton (2020) can also minimize the effect of sidelobes (Fig. 7f). This procedure is used to minimize the masking effects of the effective source time function by subtracting the average from each autocorrelation trace (Fig. 7b & 7c). However, the intensity and wavelength of sidelobes are highly dependent on the frequency bandwidth of the autocorrelation function rather than the structure or noise. So the sidelobes effect can be considered as a specific source time function, which can be also minimized. But this procedure will diminish the reflections from the laterally invariant structure. It is unavoidable

Fig. 6. The comparison of the results of the HVSR method and correlation methods (from northwest to southeast). Red and blue plus signs represent the two-way traveltime of the reflection signals from autocorrelation and cross-correlation methods, respectively. The black circles represent the inverse of the resonant frequencies from the HVSR method. (For interpretation of the references to colour in this figure legend, the reader is referred to the web version of this article.)
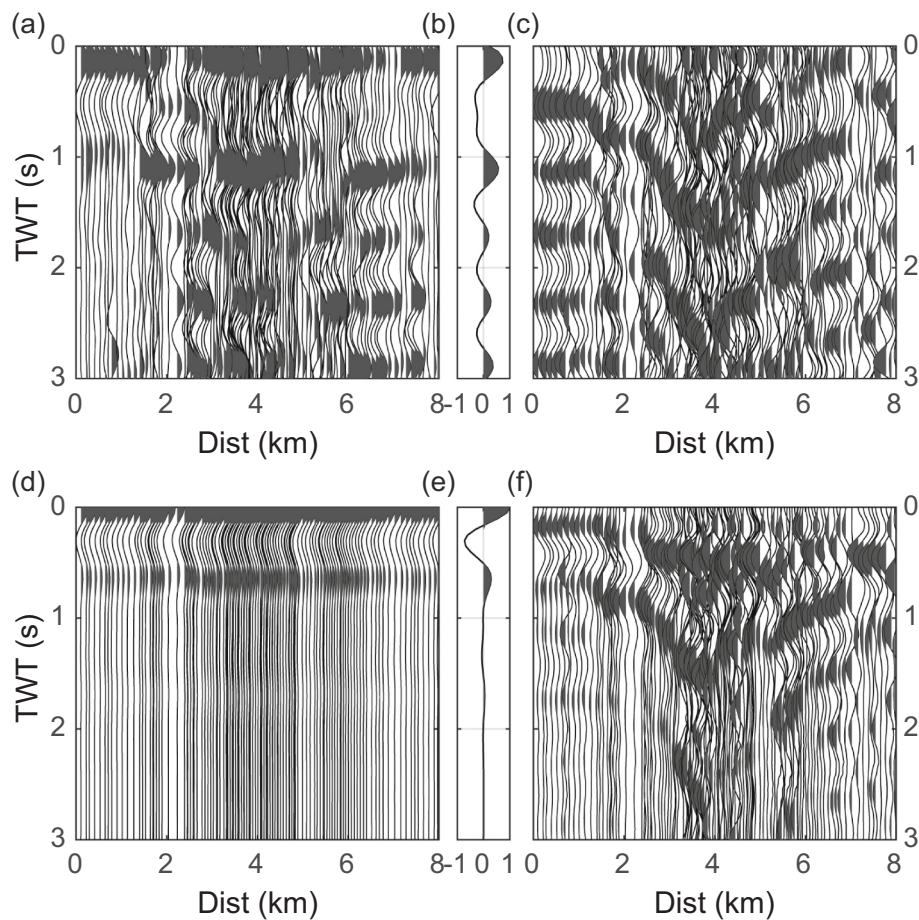
Fig. 7. (a) Results of autocorrelations with applying the cosine taper (same as Fig. 4a). (b) The average autocorrelation of all traces in (a). (c) Results of subtracting the average (b) from each autocorrelation trace in (a). (d) Results of autocorrelations without applying the cosine taper. (e) The average autocorrelation of all traces in (d). (f) Results of subtracting the average (e) from each autocorrelation trace in (d).

since we used the average autocorrelations to estimate the source time function. The horizontal structure will also be included in the estimate, and hence will be removed from the image. Therefore, we recommend the second approach for a dipping interface and the first approach for a horizontal interface. Compared with autocorrelation functions, the cross-correlation functions are less affected by sidelobes. For example, the P wave reflection signals can be detected at ~0.7 s (at ~1.5 km) in autocorrelograms (Fig. 4), while the arrivals are ~0.2 s at the same station in cross-correlograms. The results between 0 s – 0.7 s in auto-correlograms have highly interfered with the sidelobes so that we can not see clear reflections in this time range.

In this study, we use a dense linear array deployed crossing the CHF. This preeminent array system provides a good opportunity to explore the fault zone structure and to constrain the depth extent of the fault LVZ. Most autocorrelation or cross-correlation studies used a 2-D seismic array with large interstation distances to obtain a basement map (e.g. Taylor et al., 2016; Romero and Schimmel, 2018). The reflection response usually has low lateral coherence because of large interstation distances and variable interface structures, which leads to difficulties for the interpretation of the imaging results. A denser station deployment, as we used in this study, can provide more coherent reflection responses for neighboring stations, which permits us to better track reflectors laterally and to obtain the depth variations of these reflectors (Fig. 4). An inverted trapezoidal LVZ is recovered for the CHF area, which agrees well with the ambient noise tomography and teleseismic travel time analysis results (Yang et al., 2020). Indeed, a 2-D seismic network was deployed in Binchuan in 2017 with interstation distance of ~2 km (Jiang et al., 2020; Yang et al., 2021), which could be used with the

autocorrelation technique to derive the basin structure.

In this study, the low-frequency peak of HVSR curves are only used as a supporting evidence for the results from ambient noise correlation methods. We should point out that there is more useful information we can exploit from HVSR, for example, using inversion technique to generate a 2D velocity model from the HVSR curve (e.g., Rivet et al., 2015; Piña-Flores et al., 2017), comparing the HVSR curves from forward computation with the observations (e.g. García-Jerez et al., 2016), and even using the directional HVSR to observe the direction of the seismic site responses (Del Gaudio et al., 2008; Di Naccio et al., 2017; Song and Yang, 2022). We also note that the correlation method has a limited lateral resolution beneath the array. To derive higher resolution subsurface structure, spectral ratios between records at different stations of the array can be calculated, as shown in a recent study of our Binchuan array (Song and Yang, 2022). In future work, these methods can be utilized to better constrain the fault properties of the CHF and underground structure in other regions with dense seismic network. and

5. Conclusions

In this study, we have shown that correlation methods and the HVSR method are useful to image the interface of LVZ in the CHF area. An inverted trapezoidal LVZ which extends to ~1.0 km depth with a lateral extent of ~3 km is constrained in our study. Neither active sources nor earthquakes are needed in these methods. Only one-month continuous seismic records were collected and processed to derive such results. The dense station deployment of the linear array enables high lateral resolution of the interface imaging results and enhances the reliability and

stability of our results. These kinds of dense array observation systems are recommended in imaging fault zone structures in future studies.

Funding

Data availability statement

Waveform data used in this study are available from Data Management Centre of China Seismic Experimental Site (http://www.cses.ac.cn).

Declaration of Competing Interest

The authors declare no conflict of interest.

References

Allam, A.A., Ben-Zion, Y., 2012. Seismic velocity structures in the southern California plate-boundary environment from double-difference tomography. Geophys. J. Int. 190, 1181–1196.

Allen, C.R., Gillespie, A.R., Yuan, H., Sieh, K.E., Buchun, Z., Chengnan, Z., 1984. Red River and associated faults, Yunnan province, China: Quaternary geology, slip rates, and seismic hazard. Geol. Soc. Am. Bull. 95 (6), 686–700.

Arai, H., Tokimatsu, K., 2004. S-Wave velocity profiling by inversion of microtremor H/V spectrum. Bull. Seismol. Soc. Am. 94 (1), 53–63.

Bao, F., Li, Z., Yuen, D.A., Zhao, J., Ren, J., Tian, B., Meng, Q., 2018. Shallow structure of the Tangshan fault zone unveiled by dense seismic array and horizontal-to-vertical spectral ratio method. Phys. Earth Planet. Inter. 281, 46–54.

Bensen, G., Ritzwoller, M., Barmin, M., Levshin, A., Lin, F., Moschetti, M., Shapiro, N.M., Yang, Y., 2007. Processing seismic ambient noise data to obtain reliable broad-band surface wave dispersion measurements. Geophys. J. Int. 169 (3), 1239–1260. https://doi.org/10.1111/j.136 5-246X.2007.03374.x.

Ben-Zion, Y., Aki, K., 1990. Seismic radiation from an SH line source in a laterally heterogeneous planar fault zone. Bull. Seismol. Soc. Am. 80, 971–994.

Ben-Zion, Y., Ampuero, J.-P., 2009. Seismic radiation from regions sustaining material damage. Geophys. J. Int. 178 (3), 1351–1356. https://doi.org/10.1111/j.1365-246X.2009.04285.x.

Ben-Zion, Y., Malin, P., 1991. San Andreas fault zone head wave near Parkfield, California. Science 251, 1592–1594.

Ben-Zion, Y., Sammis, C.G., 2003. Characterization of fault zones. Pure Appl. Geophys. 160 (3), 677–715. https://doi.org/10.1007/PL00012554.

Ben-Zion, Y., Sammis, C.G., 2009. Mechanics, structure and evolution of fault zones. Pure Appl. Geophys. 166 (10–11), 1533–1536. https://doi.org/10.1007/s00024-009-0509-y.

Ben-Zion, Y., Shi, Z., 2005. Dynamic rupture on a material interface with spontaneous generation of plastic strain in the bulk. Earth Planet. Sci. Lett. 236, 486–496.

Bodin, P., Smith, K., Horton, S., Hwang, H., 2001. Microtremor observations of deep sediment resonance in metropolitan memphis, Tennessee. Eng. Geol. 62 (1), 159–168.

Bonnefoy-Claudet, S., Cotton, F., Bard, P.Y., 2006. The nature of noise wavefield and its applications for site effects studies: a literature review. Earth Sci. Rev. 79 (3–4), 205–227.

Brocher, T.M., 2005. Empirical relations between elastic wavespeeds and density in the Earth's crust. Bull. Seismol. Soc. Am. 95 (6), 2081–2092.

Budny, M., 1985. Seismische Bestimmung der Bodendyna-mischen Kennwerte von oberflächennahen Schichten in Erdbebengebieten der niederrheinischen Bucht undihre inge-nieurseismologische Anwendung, Sonderver off. Geology Institute of University of Köln, p. 208.

Chandler, V.W., Lively, R.S., 2016. Utility of the horizontal-to-vertical spectral ratio passive seismic method for estimating thickness of quaternary sediments in Minnesota and adjacent parts of Wisconsin. Interpretation 4 (3). SH71–SH90.

Chen, X., Yang, H., 2020. Effects of seismogenic width and low-velocity zones on estimating slip-weakening distance from near-fault ground deformation. Geophys. J. Int. 223 (3), 1497–1510. https://doi.org/10.1093/gji/ggaa385.

Chester, F.M., Evans, J.P., Biegel, R.L., 1993. Internal structure and weakening mechanisms of the San Andre as Fault. J. Geophys. Res. 98 (771–786), B01866. https://doi.org/10.1029/92J.

Clayton, R.W., 2020. Imaging the subsurface with ambien t noise autocorrelations. Seismol. Res. Lett. XX, 1–6. https://doi.org/10.1785/0220190272.

Del Gaudio, V., Coccia, S., Wasowski, J., Gallipoli, M.R., Mucciarelli, M., 2008. Detection of directivity in seismic site response from microtremor spectral analysis. Nat. Hazards Earth Syst. Sci. 8, 751–762.

Di Naccio, D., Vassallo, M., Giulio, G.D., Amoroso, S., Cantore, L., Hailemikael, H., Falcuccici, E., Gori, S., Milana, G., 2017. Seismic amplification in a fractured rock site. The case study of San Gregorio (L'Aquila, Italy). Phys. Chem. Earth Parts A/B/C 98, 90–106.

Dor, O., Rockwell, T.K., Ben-Zion, Y., 2006. Geologic observations of damage asymmetry in the structure of the San Jacinto, San Andreas and Punchbowl faults in southern California: a possible indicator for preferred rupture propagation direction. Pure Appl. Geophys. 163, 301–349. https://doi.org/10.1007/s0002 4-005-0023-9.

Eberhart-Phillips, D., Stanley, W.D., Rodriguez, B.D., Lutter, W.J., 1995. Surface seismic and electrical methods to detect fluids related to faulting. J. Geophys. Res. 100 (B7). https://doi.org/10.1029/94JB03256, 12, 919–12, 936.

Fan, C., Wang, G., Wang, S.F., Wang, E., 2006. Structural interpretation of extensional deformation along the Dali Fault System, Southeastern margin of the Tibetan Plateau. Int. Geol. Rev. 48 (4), 287–310.

Faulkner, D.R., Jackson, C.A.L., Lunn, R.J., Schlische, R.W., Shipton, Z.K., Wibberley, C. A.J., Withjack, M.O., 2010. A review of recent developments concerning the structure, mechanics and fluid flow properties of fault zones. J. Struct. Geol. 32 (11), 1557–1575. https://doi.org/10.1016/j.jsg.2010.06.009.

Feng, J., Yao, H., Poli, P., Fang, L., Wu, Y., Zhang, P., 2017. Depth variations of 410 km and 660 km discontinuities in eastern North China Craton revealed by ambient noise interferometry. Geophys. Res. Lett. 44, 8328–8335. https://doi.org/10.1002/2017GL074263.

García-Jerez, A., Piña-Flores, J., Sánchez-Sesma, F.J., Luzón, F., Perton, M., 2016. A computer code for forward computation and inversion of the H/V spectral ratio under the diffuse field assumption. Comput. Geosci. 97, 67–78. https://doi.org/10.1016/j.cageo.2016.06.016.

Gu, N., Wang, K., Gao, J., Ding, N., Yao, H., Zhang, H., 2019. Shallow crustal structure of the Tanlu fault zone near Chao Lake in eastern China by direct surface wave tomography from local dense array ambient noise analysis. Pure Appl. Geophys. 176 (3), 1193–1206. https://doi.org/10.1007/s00024-018-2041-4.

Hillers, G., Campillo, M., Ben-Zion, Y., Roux, P., 2014. Seismic fault zone trapped noise. J. Geophys. Res. Solid Earth 119, 5786–5799. https://doi.org/10.1002/2014JB011217.

Huang, Y., Ampuero, J.P., Helmberger, D.V., 2014. Earthquake ruptures modulated by waves in damaged fault zones. J. Geophys. Res. Solid Earth 119, 3133–3154. https://doi.org/10.1002/2013JB010724.

Huang, X.J., Wu, Z., Huang, X., Luo, R., 2018a. Tectonic geomorphology constrains on the quaternary activity and segmentation along Chenghai-Binchuan fault zone in Northwest Yunnan, China. Earth Sci. 43 (12), 4651. https://doi.org/10.3799/dqkx.2017.548.

Huang, X.L., Wu, Z.H., Wu, K.G., 2018b. Surface Rupture of the 1515 Yongsheng Earthquake in Northwest Yunnan, and its Seismogeological Implications. Acta Geologica Sinica(English Edition) 92 (04), 42–51.

Jiang, X., Hu, S., Yang, H., 2021. Depth extent and Vp/Vs ratio of the Chenghai fault zone, Yunnan, China constrained from dense-array-based teleseismic receiver functions. J. Geophys. Res. Solid Earth 126. https://doi.org/10.1029/2021JB022190 e2021JB022190.

Jiang, X., Yang, H., Yang, W., Wang, W., 2020. Crustal structure in the Binchuan basin of Yunnan constrained from receiver functions on a 2-D seismic dense array. Earthq. Sci. 33, 264–272. https://doi.org/10.29382/eqs-2020-0264-01.

Kennett, B.L.N., Saygin, E., Salmon, M., 2015. Stacking autocorrelograms to map Moho depth with high spatial resolution in southeastern Australia. Geophys. Res. Lett. 42, 7490–7497. https://doi.org/10.1002/2015GL065345.

Li, Y.G., Leary, P., Aki, K., Malin, P., 1990. Seismic trapped modes in the Oroville and San Andreas Fault zones. Science 249, 763–766.

Li, H., Zhu, L., Yang, H., 2007. High-resolution structures of the Landers fault zone inferred from aftershock waveform data. Geophys. J. Int. 171, 1295–1307.

Li, H., Wang, H., Xu, Z., Si, J., Pei, J., Li, T., Huang, Y., Song, S., Kuo, L., Sun, Z., Chevalier, M.L., Liu, D., 2013. Characteristics of the fault-related rocks, fault zones and the principal slip zone in the Wenchuan earthquake fault scientific drilling project Hole–1 (WFSD–1). Tectonophysics 584, 23–42. https://doi.org/10.1016/j.tecto.2012.08.021.

Li, C., Yao, H., Yang, Y., Luo, S., Wang, K., Wan, K., Wen, J., Liu, B., 2020. 3-D shear velocity structure in the shallow crust of Tanlu fault zone in Lujiang, Anhui, and adjacent areas and its tectonic implication. Earth Planetary Physics 4 (3), 317–328. https://doi.org/10.26464/epp2020026.

Lin, F., Li, D., Clayton, R.W., Hollis, D., 2013. High-resolution 3D shallow crustal structure in Long Beach, California: application of ambient noise tomography on a dense seismic array. Geophysics 78 (4), Q45–Q56. https://doi.org/10.1190/GEO2012-0453.1.

Molnar, S., Cassidy, J.F., Castellaro, S., Cornou, C., Crow, H., Hunter, J.A., Matsushima, S., Sánchez-Sesma, F.J., Yong, A., 2018. Application of microtremor horizontal-to-vertical spectral ratio (MHVSR) analysis for site characterization: State of the art. Surv. Geophys. 39 (4), 613–631.

Nakamura, Y., 1989. A method for dynamic characteristics estimation of subsurface using microtremor on the ground surface. Quart. Report Rtri 30 (1), 25–33.

Parolai, S., Bormann, P., Milkereit, C., 2002. New relationships between Vs, thickness of sediments, and resonance frequency calculated by the H/V ratio of seismic noise for the Cologne area (Germany). Bull. Seismol. Soc. Am. 92 (6), 2521–2527.

Piña-Flores, J., Perton, M., García-Jerez, A., Carmona, E., Luzón, F., Molina-Villegas, J. C., Sánchez-Sesma, F.J., 2017. The inversion of spectral ratio H/V in a layered system using the diffuse field assumption (DFA). Geophys. J. Int. 208, 577–588. https://doi.org/10.1093/gji/ggw416.

Qian, R., Liu, L., 2020. Imaging the active faults with ambient noise passive seismics and its application to characterize the Huangzhuang-Gaoliying fault in Beijing Area, northern China. Eng. Geol. 105520 https://doi.org/10.1016/j.enggeo.2020.105520.

Rivet, D., Campillo, M., Sánchez-Sesma, F., Shapiro, N.M., Singh, S.K., 2015. Identification of surface wave higher modes using a methodology based on seismic noise and coda waves. Geophys. J. Int. 203, 856–868. https://doi.org/10.1093/gji/ggv339.

Romero, P., Schimmel, M., 2018. Mapping the basement of the Ebro Basin in Spain with seismic ambient noise autocorrelations. *Journal of Geophysical Research: Solid.* Earth 123. https://doi.org/10.1029/2018JB015498.

Ruigrok, E., Wapenaar, K., 2012. Global-phase seismic interferometry unveils P wave reflectivity below the Himalayas and Tibet. Geophys. Res. Lett. 39, L11303. https://doi.org/10.1029/2012GL051672.

Sánchez-Sesma, F.J., Rodríguez, M., Iturrarán-Viveros, U., Luzón, F., Campillo, M., Margerin, L., García-Jerez, A., Suarez, M., Santoyo, M.A., Rodríguez-Castellanos, A., 2011. A theory for microtremor H/V spectral ratio: application for a layered medium. Geophys. J. Int. 186 (1), 221–225.

Saygin, E., Cummins, P.R., Lumley, D.E., 2017. Retrieval of the P wave reflectivity response from autocorrelation of seismic noise: Jakarta Basin, Indonesia. Geophys. Res. Lett. 44, 792–799. https://doi.org/10.1002/2016GL071363.

Schimmel, M., Paulssen, H., 1997. Noise reduction and detection of weak, coherent signals through phase-weighted stacks. Geophys. J. Int. 130 (2), 497–505. https://doi.org/10.1111/j.1365-246X.1997.tb05664.x.

Schimmel, M., Stutzmann, E., Gallart, J., 2011. Using instantaneous phase coherence for signal extraction from ambient noise data at a local to a global scale. Geophys. J. Int. 184 (1), 494–506. https://doi.org/10.1111/j.1365-246X.2010.04861.x.

Seht, I.V., Wohlenberg, Jürgen, 1999. Microtremor measurements used to map thickness of soft sediments. Bull. Ssmological Soc. Am. 89 (1).

Shen, Z., Lü, J., Wang, M., Bürgmann, R., 2005. Contemporary crustal deformation around the southeast borderland of the Tibetan Plateau. J. Geophys. Res. Solid Earth 110 (B11), 1–17.

Song, J., Yang, H., 2022. Seismic site response inferred from records at a Dense Linear Array across the Chenghai Fault Zone, Binchuan, Yunnan. J. Geophys. Res. 127 (1) https://doi.org/10.1029/2021JB022710.

Taylor, G., Rost, S., Houseman, G., 2016. Crustal imaging across the North Anatolian Fault Zone from the autocorrelation of ambient seismic noise. Geophys. Res. Lett. 43, 2502–2509. https://doi.org/10.1002/2016GL067715.

Thurber, C., Zhang, H.J., Waldhauser, F., Hardebeck, J., Micheal, A., Eberhart-Phillips, D., 2006. Three-dimensional compressional wavespeed model, earthquake relocations, and focal mechanisms for the Parkfield, California, region. Bull. Seismol. Soc. Am. 96 (4B), S38–S49.

Tuan, T.T., Vinh, P.C., Malischewsky, P., Aoudia, A., 2016a. Approximate formula of peak frequency of h/v ratio curve in multilayered model and its use in h/v ratio technique. Pure Appl. Geophys. 173 (2), 487–498.

Tuan, T.T., Vinh, P.C., Ohrnberger, M., Malischewsky, P., Aoudia, A., 2016b. An improved formula of fundamental resonance frequency of a layered half-space model used in h/v ratio technique. Pure Appl. Geophys. 173 (8), 1–10.

Vassallo, M., Festa, G., Bobbio, A., Serra, M., 2016. Low shear velocity in a normal fault system imaged by ambient noise cross correlation: the case of the Irpinia fault zone, Southern Italy. J. Geophys. Res. Solid Earth 121, 4290–4305. https://doi.org/10.1002/2015JB012410.

Wang, E., Burchfiel, B., Royden, L., Chen, L., Chen, J., Li, W., Chen, Z., 1998. Late Cenozoic Xianshuihe/Xiaojiang and Red River fault systems of southwestern Sichuan and Central Yunnan, China. Special Paper of the Geological Society of America 327, 1–108.

Weng, H., Yang, H., Zhang, Z., Chen, X., 2016. Earthquake rupture extents and coseismic slips promoted by damaged fault zones. J. Geophys. Res. Solid Earth 121, 4446–4457. https://doi.org/10.1002/2015JB012713.

Yang, H., 2015. Recent advances in imaging crustal fault zones: a review. Earthq. Sci. 28 (2), 151–162.

Yang, H., Yao, S., 2021. Shallow destructive earthquakes. Earthq. Sci. 34 (1) https://doi.org/10.29382/eqs-2020-0072.

Yang, H., Zhu, L., 2010. Shallow low-velocity zone of the San Jacinto fault from local earthquake waveform modeling. Geophys. J. Int. 183 (1), 421–432. https://doi.org/10.1111/j.1365-246X.2010.04744.x.

Yang, H., Duan, Y., Song, J., Wang, W., Tian, X., et al., 2021. Illuminating high-resolution crustal fault zones and temporal changes using multi-scale dense arrays and airgun sources. Earthquake Res. Adv. 1 (1), 100001 https://doi.org/10.19743/j. cnki.0891-4176.202101002.

Yang, H., Li, Z., Peng, Z., Ben-Zion, Y., Vernon, F., 2014. Low velocity zones along the San Jacinto Fault, Southern California, from body waves recorded in dense linear arrays. J. Geophys. Res. Solid Earth 119, 8976–8990. https://doi.org/10.1002/2014JB011548.

Yang, H., Duan, Y., Song, J., Jiang, X., Tian, X., Yang, W., Wang, W., Yang, J., 2020. Fine structure of the Cheng hai fault zone, Yunnan, China, constrained from teleseismic travel time and ambient noise tomography. *Journal of Geophysical Research: Solid.* Earth 125. https://doi.org/10.1029/2020JB019565 e2020JB019565.

Zelt, B., Ellis, R., 1999. Receiver-function studies in the Trans-Hudson Orogen, Saskatchewan[J]. Can. J. Earth Sci. 36 (4), 585–603.

Zhang, J., Gerstoft, P., 2014. Local-scale cross-correlation of seismic noise from the calico fault experiment. Earthq. Sci. 27, 311–318. https://doi.org/10.1007/s11589-014-0074-z.

Zhang, P., Shen, Z., Wang, M., Gan, W., Bürgmann, R., Molnar, P., Wang, Q., Niu, Z., Sun, J., Wu, J., Sun, H., You, X., 2004. Continuous deformation of the Tibetan plateau from global positioning system data. Geology 32 (9), 809–812.

Zigone, D., Ben-Zion, Y., Campillo, M., Roux, P., 2014. Seismic tomography of the Southern California plate boundary region from noise-based Rayleigh and love waves. Pure Appl. Geophys. https://doi.org/10.1007/s00024-014-0872-1.

Zigone, D., Ben-Zion, Y., Lehujeur, M., Campillo, M., Hillers, G., Vernon, F.L., 2019. Imaging subsurface structures in the San Jacinto fault zone with high-frequency noise recorded by dense linear arrays. Geophys. J. Int. 217 (2), 879–893. https://doi.org/10.1093/gji/ggz069.